Charge-Orbital Density Wave and Superconductivity in the Strong Spin-Orbit Coupled IrTe₂:Pd

J. J. Yang,[1,2] Y. J. Choi,[3] Y. S. Oh,[3] A. Hogan,[3] Y. Horibe,[3] K. Kim,[2] B. I. Min,[2] and S-W. Cheong[1,2,3,*]

[1]*Laboratory for Pohang Emergent Materials, Pohang University of Science and Technology, Pohang 790-784, Korea*
[2]*Department of Physics, Pohang University of Science and Technology, Pohang 790-784, Korea*
[3]*Rutgers Center for Emergent Materials and Department of Physics & Astronomy, Rutgers University,
Piscataway, New Jersey 08854, USA*

Using transmission electron microscopy, the anomalies in resistivity and magnetic susceptibility at ~ 262 K in IrTe₂ are found to accompany the superlattice peaks with $\vec{q} = (1/5, 0, -1/5)$. The wave vector is consistent with our theoretical calculation for the Fermi surface nesting vector, indicating that the ~ 262 K transition is of the charge-orbital density wave (DW) type. We also discovered that both Pd intercalation and substitution induce bulk superconductivity with T_c up to ~ 3 K, which competes with DW in a quantum critical pointlike manner.

Materials with large spin-orbital (SO) coupling have attracted phenomenal attention in condensed matter physics and materials science communities. Large SO coupling is a prerequisite for hard magnets (such as SmCo₅ [1] and FePt [2]) with large magnetic anisotropy [3] or multiferroics (such as orthorhombic HoMnO₃ [4]) with large magnetism-induced polarizations [5]. Furthermore, large SO coupling can result in unique quantum states such as $J_{\mathrm{eff}} = 1/2$ Mott insulators, such as Sr₂IrO₄, where spin and orbital degrees of freedom are strongly entangled [6], or topological insulators, such as Bi₂Se₃ and Bi₂Te₃ [7,8]. Topological insulators are materials with finite band gaps in which large SO coupling induces band inversion, so topological metallic surface states with Dirac conelike dispersions, protected by time reversal symmetry, appear [9–11]. Furthermore, nonconventional superconductivity pairing can be present in the so-called topological superconductors with large SO coupling [12–14]. Cu-intercalated Bi₂Se₃ (Cu$_x$Bi₂Se₃) is a candidate for the topological superconductors [15–19]. It will be highly valuable to discover new superconductors with large SO coupling in order to understand the nature of topological superconductivity. Note that SO coupling is proportional to Z^4, where Z is the atomic number, and further exploration of materials with large Z's may lead to new quantum states or novel functionalities.

Because of large Z, IrTe₂ must be associated with huge SO coupling, which is expected to be comparable with that of topologically insulating Bi₂Se₃. Interestingly, IrTe₂ exhibits an intriguing phase transition at ~ 250 K, where distinct anomalies of resistivity and magnetic susceptibility were observed [20], but the exact nature of the transition has been little studied. We discovered that the phase transition is of the charge-orbital density wave (DW) type, and superconductivity with T_c up to ~ 3 K sets in as soon as the DW transition is suppressed by the intercalation (Pd$_x$IrTe₂) or Ir-site doping (Ir$_{1-y}$Pd$_y$Te₂) of a small

amount of Pd. We emphasize that both Pd$_x$IrTe₂ and Ir$_{1-y}$Pd$_y$Te₂, near the optimal concentrations, exhibit full magnetic shielding below T_c and complete superconducting transitions in resistance-temperature curves, indicating bulk intrinsic superconductivity. On the contrary, Cu$_x$Bi₂Se₃, a candidate for the topological superconductors, tends to show a poor superconducting transition [15–17]. Thus, Pd$_x$IrTe₂ and Ir$_{1-y}$Pd$_y$Te₂ may be better systems to explore the possibility of topological superconductivity.

Polycrystalline specimens of Pd$_x$IrTe₂ and Ir$_{1-y}$Pd$_y$Te₂ were prepared using 99.95% Ir, 99.99% Te, and 99.99% Pd. Stoichiometric quantities of the elements were mixed, ground, and pelletized. Then, the pellets were placed in quartz tubes and sealed under a vacuum. The pellets were sintered at 1000 °C for 15 hours, followed by furnace cooling to room temperature. The process was repeated twice with an intermediate grinding. The results of x-ray diffraction, performed using a Rigaku D/Max-RB x-ray diffractometer with a Cu K_α radiation, show that all specimens are in single phase. Magnetic and electrical transport properties were measured using the Quantum Design MPMS-XL7 and PPMS-9. The specimens for the transmission electron microscope (TEM) experiments were prepared with gentle crushing of the pellets. The observations were carried out with the JEOL-2010F and JEOL-2000FX TEMs equipped with a liquid-nitrogen-cooled holder. The structural change in IrTe₂ was investigated with observing electron diffraction (ED) patterns upon cooling. Note that the indexes in the ED patterns are based on the trigonal structure.

IrTe₂ is a layered compound with trigonal symmetry ($P\bar{3}m1$), as shown in Fig. 1(a). Ir ions are octahedrally coordinated with six Te ions, and the face sharing of Ir-Te₆ cages forms IrTe₂ layers. Different from typical layered transitional metal dichalcogenides, IrTe₂ layers are bonded to each other by significant "Te-Te bonding," rather than
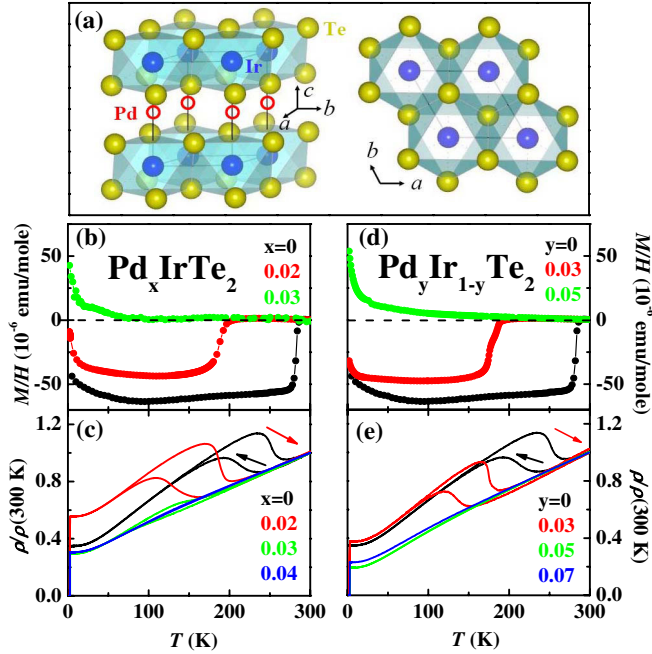
FIG. 1 (color online). (a) Lattice structure of IrTe$_2$.
(b) Temperature-dependent magnetic susceptibility for
Pd$_x$IrTe$_2$ ($0 \le x \le 0.03$) in $H = 2$ T. (c) Temperature-
dependent resistivity for Pd$_x$IrTe$_2$ ($0 \le x \le 0.04$) (normalized
at 300 K). (d) Temperature-dependent magnetic susceptibility
for Ir$_{1-y}$Pd$_y$Te$_2$ ($0 \le y \le 0.05$) in $H = 2$ T. (e) Temperature-
dependent resistivity for Ir$_{1-y}$Pd$_y$Te$_2$ ($0 \le y \le 0.07$) (normal-
ized at 300 K). Black and light gray (red) arrows indicate the
cooling and heating processes, respectively.

weak van der Waals force [21]. However, the IrTe$_2$ crystals
are highly cleavable along IrTe$_2$ layers, and Pd ions can be
intercalated between IrTe$_2$ layers [see the schematics of the
intercalated Pd ions in the left panel of Fig. 1(a)]. This
results in a monotonic increase of the c lattice parameter
with increasing Pd content in Pd$_x$IrTe$_2$, as evinced by our
refined lattice parameters (see S1 of the Supplemental
Material [22]) [23]. For Pd-substituted Ir$_{1-y}$Pd$_y$Te$_2$, part
of the Ir ions in the IrTe$_2$ layer are replaced by Pd ions.
Considering the fact that the a lattice parameter of PdTe$_2$
(4.034 Å) is larger than that of IrTe$_2$ (3.930 Å) and the c
lattice parameter of PdTe$_2$ (5.132 Å) is smaller than that of
IrTe$_2$ (5.386 Å), Pd substitution into IrTe$_2$ will result in the
increase of a and decrease of c [24], consistent with our
refinement results of Ir$_{1-y}$Pd$_y$Te$_2$ (see S1 of the
Supplemental Material [22]).

   Figures 1(b) and 1(c) show the temperature dependence
of magnetic susceptibility and resistivity for Pd$_x$IrTe$_2$.
Consistent with previous reports, pure IrTe$_2$ exhibits a
200–280 K transition with a large thermal hysteresis ac-
companying a magnetic susceptibility drop and resistivity
increase upon cooling. When 2% Pd is intercalated into
IrTe$_2$, the transition is significantly suppressed to 120–
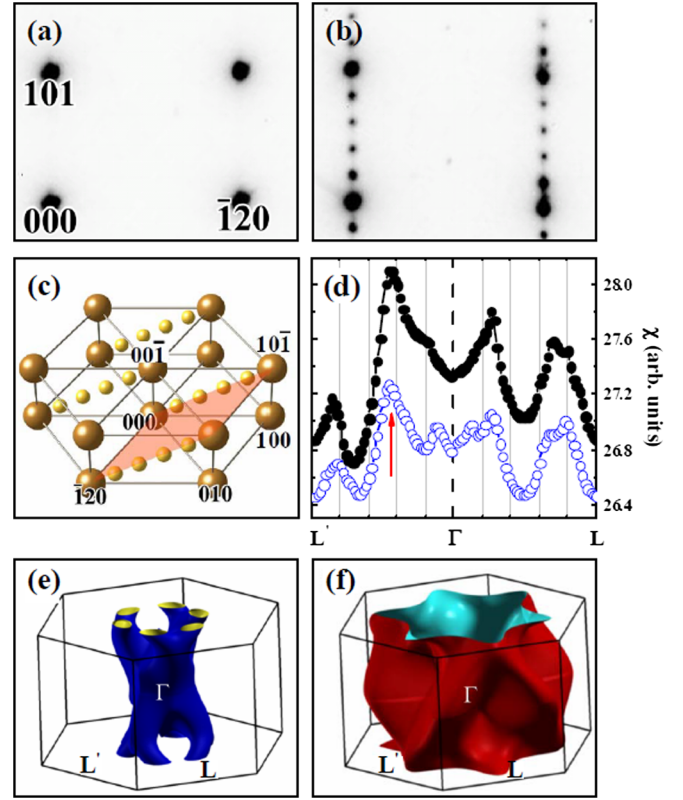190 K and the magnitude of the magnetic susceptibility

FIG. 2 (color online).   (a) Electron diffraction pattern of IrTe$_2$
at 284 K. (b) Electron diffraction pattern of IrTe$_2$ at 84 K.
(c) Reciprocal lattice of IrTe$_2$ at 84 K. Big balls represent
the fundamental lattice, and small balls correspond to the
superlattice. (d) The charge susceptibility $\chi(\vec{q})$ along
$L'(1/2, 0, -1/2)$-Γ-$L(0, 1/2, 1/2)$. The dominating peak is at
$\vec{q} = (\sim 1.1/5, 0, \sim -1.1/5)$ (red arrow). Solid (black) circles
are the data calculated without SO coupling, and open (blue)
circles represent the data with SO coupling. (e) Inner and
(f) outer Fermi surfaces of IrTe$_2$.

drop decreases. For 3% Pd intercalation, a hint of the
transition exists at 70–150 K and the transition appears to
be absent at 4% Pd intercalation. Figures 1(d) and 1(e)
exhibit the temperature dependence of magnetic suscepti-
bility and resistivity for doped Ir$_{1-y}$Pd$_y$Te$_2$. Pd substitution
suppresses the transition in a manner slightly slower than
that for Pd intercalation. For $y = 0.03$, the transition is
suppressed to 130–180 K and is not visible at $y = 0.05$. A
sudden increase of resistivity exists at the transition, but the
temperature dependence below the transition temperature
remains metallic, suggesting that a partial gap opens at the
Fermi level below the transition.

   The resistivity and magnetic susceptibility behavior at
the transition in IrTe$_2$ is reminiscent of the formation of
charge DWs [20]. Nevertheless, the result of an NMR
experiment did not provide any evidence for charge DW
order [25]. Matsumoto *et al.* proposed that the transition is
due to the crystallographic deformation from high tem-
perature $P\bar{3}m1$ to low temperature $C2/m$ [20]. In order to

clarify the origin of the transition, ED experiments were performed at low temperatures. Figure 2(a) shows an ED pattern of IrTe$_2$ taken at ~284 K above the transition. The peaks in Fig. 2(a) are consistent with the fundamental reciprocal lattice of the trigonal structure. Figure 2(b) displays an ED pattern with the electron incidence parallel to the [$\bar{1}$01] direction taken at 84 K below the transition. Superlattice peaks are clearly visible in the 84 K pattern and indicate the presence of a new structural modulation with the wave vector of $\vec{q} = (1/5, 0, -1/5)$ below the transition. The schematics of the new modulation wave vectors and fundamental reciprocal lattice are displayed in Fig. 2(c).

In order to unveil the origin of the new structural modulation, we have calculated the charge susceptibility $\chi(\vec{q})$:

$$\chi(\vec{q}) = \frac{1}{N} \sum_{\vec{k},n,m} \frac{f(\varepsilon_n(\vec{k}))[1 - f(\varepsilon_m(\vec{k} + \vec{q}))]}{\varepsilon_m(\vec{k} + \vec{q}) - \varepsilon_n(\vec{k}) + i\delta}.$$

The electronic structure of IrTe$_2$ for our calculation was investigated by employing the full-potential linearized augmented plane wave band method implemented in the WIEN2K code [26]. In addition, the generalized gradient approximation was adopted for the exchange correlation potential, and the spin-orbit interactions of Ir and Te ions were included in a second variation manner. As shown in Fig. 2(d), the charge susceptibility along $\Gamma(0, 0, 0)$-$L'(1/2, 0, -1/2)$ exhibits the dominant peak at ~2.2/5 of the Γ-L' length, corresponding to the wave vector of $\vec{q} = (\sim 1.1/5, 0, \sim -1.1/5)$. This indicates the presence of Fermi surface nesting at $\vec{q} = (\sim 1.1/5, 0, \sim -1.1/5)$ (see S2 in the Supplemental Material [22]), which is close to the observed superlattice peak position of $\vec{q} = (1/5, 0, -1/5)$. The small difference may originate from the commensurability effect when lattice is involved. As a comparison, the charge susceptibility calculated without SO coupling is also shown in Fig. 2(d). $\chi(\vec{q})$ without SO coupling also exhibits a dominant peak at $\vec{q} = (\sim 1.1/5, 0, \sim -1.1/5)$, but the intensity of it is slightly higher than that with SO coupling. Hence, SO coupling suppresses slightly the Fermi surface instability but does not change the wave vector. Furthermore, in materials with partially filled t_{2g} (see S2 of the Supplemental Material [22]) levels such as IrTe$_2$, an orbital degree of freedom is intricately coupled with a charge degree of freedom, and an orbitally driven Peierls instability can be responsible for a charge DW-type transition [27]. Furthermore, an orbital degree of freedom may also contribute to the commensurate locking of the superlattice modulation. Therefore, it may be legitimate to call the transition a charge-orbital DW order. It is also noteworthy that the Fermi surface of IrTe$_2$, plotted in Figs. 2(e) and 2(f), reveals rich dispersions along the c direction, reflecting the three-dimensional nature of the electronic

structure. This three-dimensional nature is consistent with our result of the partial density of states of IrTe$_2$ (see S2 of the Supplemental Material [22]).

We found that superconductivity emerges below ~3 K as soon as the DW transition is suppressed with Pd intercalation or doping, while pure IrTe$_2$ does not show superconductivity down to 0.32 K [28]. This trend is demonstrated in the low-temperature magnetic susceptibility and resistivity data shown in Fig. 3. For $x = 0.02$, diamagnetism appears below ~2.2 K [Fig. 3(a)], suggesting the onset of superconductivity. Consistently, resistivity of this sample decreases smoothly to zero around this temperature [Fig. 3(b)], suggesting bulk superconductivity. For $x = 0.03$, the bulk superconductivity is evident in the full shielding diamagnetic signal and sharp resistivity transition at 2.68 K. With further Pd intercalation, superconducting temperature (T_c) decreases, and superconductivity is no longer detectable at $x = 0.1$. Pd doping in Ir$_{1-y}$Pd$_y$Te$_2$ induces a similar trend of superconducting T_c, but at higher Pd concentrations. Weak superconductivity appears at $y = 0.03$, bulk superconductivity is optimized with $T_c = 2.99$ K at $y = 0.04$, and superconducting T_c decreases with further doping beyond $y = 0.04$
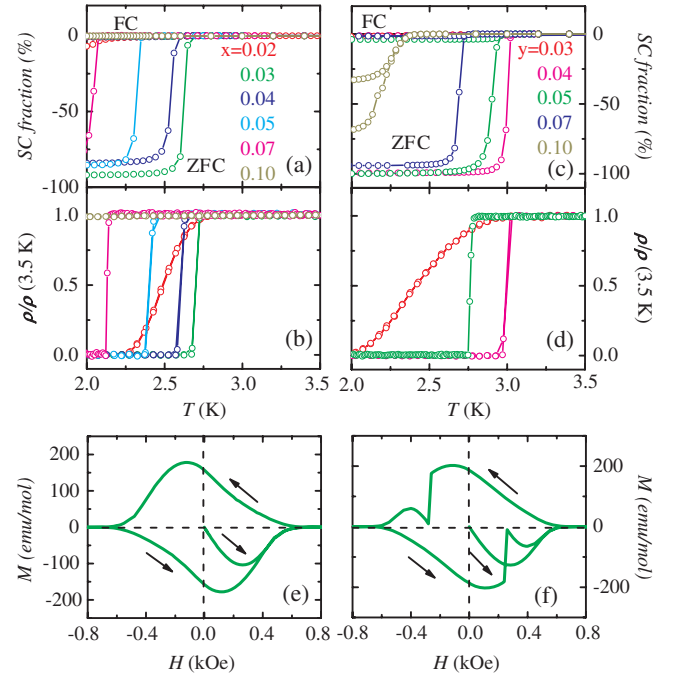

FIG. 3 (color online). (a) Temperature-dependent superconducting (SC) shielding [zero-field-cooled (ZFC)] and Meissner (FC) fraction data for Pd$_x$IrTe$_2$ ($0.02 \leq x \leq 0.1$) in $H = 10$ Oe. (b) Temperature-dependent resistivity for Pd$_x$IrTe$_2$ ($0.02 \leq x \leq 0.1$) (normalized at 3.5 K). (c) Temperature-dependent SC fraction data for Ir$_{1-y}$Pd$_y$Te$_2$ ($0.03 \leq y \leq 0.07$) in $H = 10$ Oe. (d) Temperature-dependent resistivity for Ir$_{1-y}$Pd$_y$Te$_2$ ($0.03 \leq y \leq 0.07$) (normalized at 3.5 K). (e) Magnetic hysteresis loop for Pd$_{0.03}$IrTe$_2$ at 2 K. (f) Magnetic hysteresis loop for Ir$_{0.95}$Pd$_{0.05}$Te$_2$ at 1.8 K.
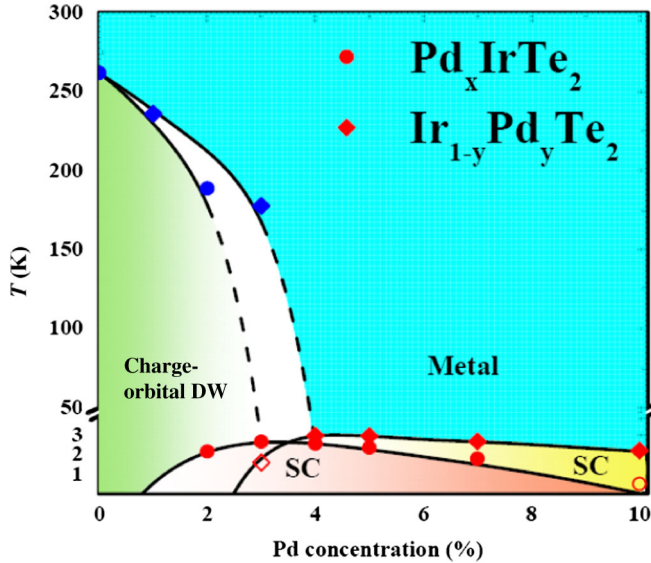
FIG. 4 (color online). (a) Electronic phase diagram of $Pd_x IrTe_2$ (circles) and $Ir_{1-y} Pd_y Te_2$ (diamonds). Dark gray (blue) symbols correspond to the DW transition temperatures, and light gray (red) symbols represent the superconducting transition temperatures. Open symbols indicate that the transition temperatures may be below our minimum available temperature.

[Figs. 3(c) and 3(d)]. Note that the magnetization data in Figs. 3(a) and 3(c) are from after the correction of the demagnetization factor of each specimen. Both intercalated and substituted specimens with nearly optimal compositions exhibit a large shielding fraction of ~100%, but Meissner fractions [i.e., field-cooled (FC) magnetization] of all specimens are negligibly small, indicating the presence of bulk superconductivity and also strong superconducting vortex pinning. For comparison, the largest reported shielding fraction of $Cu_x Bi_2 Se_3$ is only around 40% [17]. In order to reveal the detailed nature of superconductivity, magnetic hysteresis loops of $x = 0.03$ and $y = 0.05$ were measured at 2.0 and 1.8 K, respectively [Figs. 3(e) and 3(f)]. Both intercalated and substituted specimens exhibit a typical type-II superconductivity behavior. The Ginzburg-Landau parameter κ can be estimated from the following two equations, $-\int M dH = H_c^2/8\pi$ and $H_{c2} = \sqrt{2}\kappa H_c$, where M is the diamagnetic magnetization, H is the magnetic field, H_c is the thermodynamic critical field, and H_{c2} is the upper critical field. From the integration of the initial magnetization curves and the two equations above, we obtain $\kappa \approx 1.53$ for $x = 0.03$ and $\kappa \approx 1.5$ for $y = 0.05$ [29]. The sharp steps of magnetization near ± 0.25 kOe in Fig. 3(f) indicate the presence of avalanche-type flux jumps. Note that, because of the polycrystalline nature and expected poor thermal conductivity of our specimens due to the presence of heavy ions such as Ir and Te, the flux jumps can be accompanied with local heating [30].

Our results are summarized in the electronic phase diagram presented in Fig. 4. The DW transition temperature in $IrTe_2$ is strongly suppressed with Pd intercalation or substitution. As soon as DW order is significantly suppressed, superconductivity appears. The superconducting state appears for $x \geq 0.02$ (intercalation) and $y \geq 0.03$ (substitution), and superconducting T_c becomes the maximum of 2.68 K at $x = 0.03$ and of 2.99 K at $y = 0.04$, followed by T_c reduction for higher Pd concentrations. $Pd_{0.1}$-intercalated $IrTe_2$ is not superconducting down to 1.8 K. However, $Pd_{0.1}$-substituted $IrTe_2$ is still superconducting at $T_c \approx 2.3$ K, which appears consistent with the superconductivity of $PdTe_2$ at $T_c \approx 1.69$ K [28]. It is plausible that superconductivity and DW order coexist at $x = 0.02$ and $y = 0.03$ in a spatially inhomogeneous manner. A similar domelike shape of the superconducting phase boundary, where another long-range order disappears, has been observed in a number of systems, including superconducting cuprates and $Cu_x TiSe_2$ [23,31]. Barath et al. proposed that the domelike shape of $T_c(x)$ and the superconducting paring mechanism in $Cu_x TiSe_2$ stem from quantum criticality associated with fluctuations of DW order [32,33]. A similar mechanism may be active in $Pd_x IrTe_2$ and $Ir_{1-y} Pd_y Te_2$. We also note that, primarily due to large SO coupling, nonconventional superconductivity and also the presence of the Majorana surface state have been proposed in $Cu_x Bi_2 Se_3$ [15,18,34]. Since the $IrTe_2$:Pd system is expected to have a large SO coupling similar to that in $Cu_x Bi_2 Se_3$, it is quintessential to explore the possible presence of nonconventional quantum states in $IrTe_2$:Pd.

In conclusion, our results from the low-temperature TEM experiment and theoretical calculation indicate that the phase transition ~262 K in $IrTe_2$, exhibiting a sudden increase of resistivity and a drop of magnetic susceptibility upon cooling, is of the charge-orbital DW type. We discovered that bulk intrinsic superconductivity appears when DW order is suppressed with Pd intercalation or doping [35]. Superconductivity and DW order compete in a quantum critical pointlike manner. Our findings reveal the rich quantum nature of $5d$ transition metal materials with partially filled t_{2g} levels and large SO coupling and provide better systems for the exploration of topological superconductors.

*sangc@physics.rutgers.edu

[1] P. Larson, I. I. Mazin, and D. A. Papaconstantopoulos, Phys. Rev. B **67**, 214405 (2003).

[2] I. V. Solovyev, P. H. Dederichs, and I. Mertig, Phys. Rev. B **52**, 13 419 (1995).

[3] J. H. Van Vleck, Phys. Rev. **52**, 1178 (1937).

[4] N. Lee *et al.*, Phys. Rev. B **84**, 020101(R) (2011).

[5] S. W. Cheong and M. Mostovoy, Nature Mater. **6**, 13 (2007).

[6] B. J. Kim *et al.*, Phys. Rev. Lett. **101**, 076402 (2008).

[7] Y. Xia *et al.*, Nature Phys. **5**, 398 (2009).

[8] H. Zhang *et al.*, Nature Phys. **5**, 438 (2009).

[9] M. Z. Hasan and C. L. Kane, Rev. Mod. Phys. **82**, 3045 (2010).

[10] J. E. Moore, Nature (London) **464**, 194 (2010).

[11] X. L. Qi and S. C. Zhang, Rev. Mod. Phys. **83**, 1057 (2011).

[12] A. P. Schnyder *et al.*, Phys. Rev. B **78**, 195125 (2008).

[13] X. L. Qi *et al.*, Phys. Rev. Lett. **102**, 187001 (2009).

[14] J. Linder *et al.*, Phys. Rev. Lett. **104**, 067001 (2010).

[15] Y. S. Hor *et al.*, Phys. Rev. Lett. **104**, 057001 (2010).

[16] L. A. Wray *et al.*, Nature Phys. **6**, 855 (2010).

[17] M. Kriener *et al.*, Phys. Rev. Lett. **106**, 127004 (2011).

[18] L. Fu and E. Berg, Phys. Rev. Lett. **105**, 097001 (2010).

[19] M. Kriener *et al.*, Phys. Rev. Lett. **106**, 127004 (2011).

[20] N. Matsumoto *et al.*, J. Low Temp. Phys. **117**, 1129 (1999).

[21] C. S. Lee and G. J. Miller, Inorg. Chem. **38**, 5139 (1999).

[22] See Supplemental Material at http://link.aps.org/supplemental/10.1103/PhysRevLett.108.116402 for the refined lattice parameter of IrTe$_2$:Pd, and the density of states and Fermi surface nesting of IrTe$_2$.

[23] E. Morosan *et al.*, Nature Phys. **2**, 544 (2006).

[24] T. R. Finlayson, W. Reichardt, and H. G. Smith, Phys. Rev. B **33**, 2473 (1986).

[25] K. Mizuno *et al.*, Physica (Amsterdam) **312B**, 818 (2002).

[26] P. Blaha *et al.*, *WIEN2k: An Augmented Plane Wave Plus Local Orbitals Program for Calculating Crystal Properties* (Vienna University of Technology, Austria, 2001).

[27] D. I. Khomskii and T. Mizokawa, Phys. Rev. Lett. **94**, 156402 (2005).

[28] Ch. J. Raub *et al.*, J. Phys. Chem. Solids **26**, 2051 (1965).

[29] M. Tinkham, *Introduction to Superconductivity* (McGraw-Hill, New York, 1996), 2nd ed.

[30] Jae-Yeap Lee *et al.*, J. Appl. Phys. **108**, 033909 (2010).

[31] P. A. Lee, N. Nagaosa, and X-G. Wen, Rev. Mod. Phys. **78**, 17 (2006).

[32] H. Barath *et al.*, Phys. Rev. Lett. **100**, 106402 (2008).

[33] A. H. Castro Neto, Phys. Rev. Lett. **86**, 4382 (2001).

[34] L. Fu and C. L. Kane, Phys. Rev. Lett. **100**, 096407 (2008).

[35] In the review process of our Letter, after the completion of our work, we became aware of the following presentation: Sunseng Pyon *et al.*, in *Proceedings of the International Conference on Novel Superconductivity (ICNSCT2011), Taiwan, 2011* (to be published) [http://www.phys.sinica.edu.tw/~ICNS2011/download/abstract/P089.pdf].